Effect of erodent properties on the erosion of alumina

L. MURUGESH, R. O. SCATTERGOOD
Department of Materials Science and Engineering, North Carolina State University, Raleigh, NC 27695, USA

The effect of erodent particle properties for solid particle erosion in a series of alumina ceramics was investigated using alumina and SiC erodents. Using a new model analysis, the results were interpreted in terms of particle fragmentation effects and related erodent–target properties. An increase in the erosion rate with increase in the particle–target hardness ratio reported in the literature is related to these effects but is not actually a direct consequence of hardness. Changes in the velocity exponents for erosion were observed and can be explained by blunting due to crushing and fragmentation of larger erodent particles. The quasi-static model for erosion predicts a reduction in the velocity exponent as the particle-tip blunting increases. In steady state, SEM observations show that lateral crack controlled erosion mechanisms operate in all cases but, for certain combinations of erodent and target properties, damage accumulation by plastic punching occurs.

1. Introduction

Under erosive conditions, it has been suggested that the relative hardness of the erodent particles and the target material may play an important role in the erosion behaviour of brittle materials. Recent observations by Wada and co-workers [1, 2] have shown that the properties of the erodent particles affect the erosion rate and crack morphology of brittle materials. Wada and Watanabe [1] reported an increase in the erosion rates when the ratio of the hardness of the particle, H_p, to the hardness of the target, H_t, was increased. In particular, erosion rates increased markedly at a transition point $H_p/H_t = 1$. Similar changes in the overall erosion behaviour and crack morphology were noticed when the ratio of H_p/H_t was increased from unity to higher values for aluminas and SiC-reinforced alumina [2]. Impact events on these materials using alumina erodents yielded punching-type events with the absence of lateral cracking. However, when impacted with SiC particles, typical lateral crack formation was seen to occur. The velocity exponent using alumina abrasives was also very low and in the range of 1.3–1.8, compared to values of over 2 obtained for ceramics impacted with SiC. Such transitions in velocity exponents were also reported by Sykes et al. [3] on SiC whisker-reinforced alumina samples impacted with alumina erodent. It was seen that the velocity exponents decreased from 2.9 to 0.8 with increasing additions of SiC whiskers up to about 25%. When impacted with SiC, the same samples showed less change in velocity exponents [4]. Investigations by Morrison et al. [5] on the erosion of Si_3N_4 reinforced with SiC using alumina erodents, reported a lack of classical lateral cracking. A limited series of erosion tests by Srinivasan et al. [6] on commercial

aluminas of varying hardness found that alumina and SiC erodents gave different results for identical erosion conditions. An effect of the indentation load on fragmentation and crushing of individual erodent particles was recently reported [7] and the results indicated the presence of a threshold load for particle-tip crushing.

The objective of the current work was to systematically study the effect of erodent particle properties on erosion in alumina ceramics. The H_p/H_t effect reported earlier was one aspect of the work. A series of aluminas with varying hardness, and a single-crystal sapphire, were eroded using alumina and SiC erodents. Steady state erosion rates were measured and SEM observations were used to characterize single-impact events on polished surfaces and the steady state eroded surfaces. The results are discussed in the context of the quasi-static erosion model and a new adaptation of critical-depth models to analyse erodent fragmentation effects.

2. Erosion models
2.1. Lateral crack propagation
The most widely accepted mechanistic models for erosion in brittle materials are based on the propagation of lateral cracks [8, 9]. The elastic–plastic impact of a sharp particle will produce a damage zone where residual tensile forces, P, will generate and propagate subsurface, penny-shaped lateral cracks [10] as shown in Fig. 1. The erosion rate, ΔE, is given as the target volume removed per particle impact

$$\Delta E \propto c^2 h \qquad (1)$$

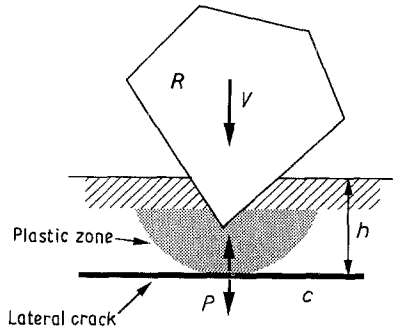where c is the equilibrium lateral crack extension and

Figure 1 Schematic of an erosion impact event.

h is the depth of formation of the lateral cracks. Assuming that c is large, the crack behaves as a centre-loaded penny crack subjected to point loading by residual forces, P. Standard fracture-mechanics analysis gives the equilibrium crack extension [11]

$$c = \frac{1}{\pi}\left(\frac{P}{K_{IC}}\right)^{2/3} \tag{2}$$

where K_{IC} represents the fracture toughness for Mode I loading. Using quasi–static analysis for the particle contact conditions [9], h scales with maximum penetration depth of the particle, z_{max}, or the mean size of the indented volume, $v_{max}^{1/3}$, while P scales with maximum contact force, F_{max},

$$h_1 \propto z_{max} \tag{3a}$$

or

$$h_2 \propto v_{max}^{1/3} \tag{3b}$$

and

$$P \propto F_{max} \tag{3c}$$

Substituting into Equation 1 for c and h, the erosion rate ΔE for normal impact is given as

$$\Delta E \propto K_{IC}^{-4/3} F_{max}^{4/3} h \tag{4}$$

where $h = h_1$ or h_2 as above. Using quasi-static analysis outlined in the Appendix to estimate F_{max} and h in terms of particle kinematics and target properties, one obtains the well-known power-law form for the erosion-rate equation

$$\Delta E = \text{constant } \rho_p^s H_t^q K_t^{-4/3} R^m V^n \tag{5}$$

where the constant is fixed for given erodent and impact angle, ρ_p, is particle density, H_t is target hardness, K_t is target fracture toughness, V is erodent velocity and R is erodent size. Note that the right-hand side of Equation 5 must be divided by $R^3 \rho_p$ to get ΔE in mass/mass units for a given target material. The exponents, s, q, n and m vary with model assumptions. Increase in the target hardness H_t increases ΔE. The size exponent $m = 2/3$ in all cases and $2/3 \le n \le 22/9$ depending on erodent particle shape and model assumptions (see Appendix). ΔE also tends to increase with ρ_p but the dependence is weak and can be ignored for the current results.

2.2. Target–particle response – fragmentation
The contact conditions between the impacting erodent

particle and the target are important in determining the target-particle response and, in particular, the propensity for erodent fragmentation on a given target. The analysis of fragmentation effects has been generally ignored in the erosion literature. Fig. 2a (left) shows the particle-target contact during impact. For an impact of a perfectly rigid indentor on to a ceramic target, the classic lateral cracking mechanism of the target occurs when the plastic zone in the target exceeds a threshold size. This reflects the fundamental scaling relationship between fracture energy and plastic work for localized deformation conditions [12]. The critical penetration depth, d_c, of the particle-into-target to initiate fracture (lateral cracking) of the target depends on the geometry of the indentor as well as the material or defect properties of the target material. Following the analysis of Lawn and Evans [13], this can be written as

$$d_c = \beta_t\left(\frac{K_t}{H_t}\right)^2\left(\frac{E_t}{H_t}\right) \tag{6}$$

where β_t is a geometric factor that will depend on indentor shape and the intrinsic flaw population in the target, K_t is the fracture toughness, H_t is the hardness and E_t is the elastic modulus of the target material. Larger flaw populations tend to reduce β because fracture initiation will be facilitated.

The indentor (erodent) is not perfectly rigid and the properties of the erodent particle cannot, in fact, be ignored. In a similar fashion to Equation 6, one can consider that the target "indents" the erodent particle
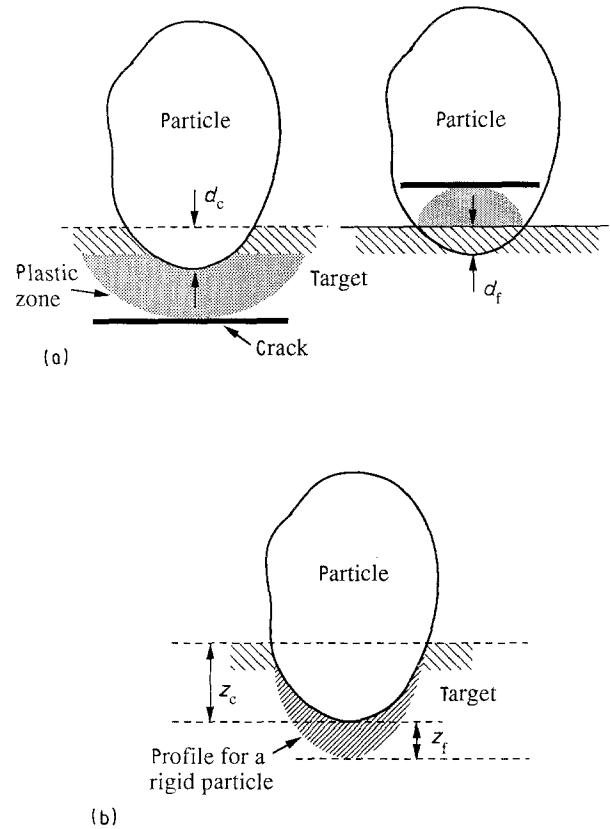

Figure 2 (a) Critical depth, d_c, to generate lateral crack in target (left) and critical depth, d_f, to generate crack in particle (right), which produces fragmentation. (b) Impact penetration depths z_c in target and z_f in particle.

as shown in Fig. 2a (right). In this case, fracture initiation will lead to fragmentation of the erodent. The critical penetration depth, d_f, of the target-into-particle to cause fracture (fragmentation) of the particle can be written as

$$d_f = \beta_p \left(\frac{K_p}{H_p}\right)^2 \left(\frac{E_p}{H_p}\right) \qquad (7)$$

where β_p is another geometric constant that depends on the intrinsic flaw population of the particle. K_p, H_p and E_p now refer to particle properties. One can expect that β_p will be particle-size dependent, i.e. larger erodent particles have a larger population of flaws (size effect), which reduces β_p.

The critical depths d_c and d_f should be normalized to account for the actual penetration depths, z, at impact. These will not be the same for the particle and target, as shown in Fig. 2b. The quasi-static analysis (see Appendix) gives the maximum particle penetration depth $z = z_{max}$ (or $v_{max}^{1/3}) \propto H_t^r$, where H_t is the hardness of the target material and $-1 \leq r \leq -1/3$, depending on particle shape and model assumptions. $D = d/z$ is a normalized measure of the ease of fracture initiation such that larger D signifies a higher resistance to fracture. $D = 1$ is the threshold condition for fracture initiation. The ratio $D_c/D_f = (d/z)_c/(d/z)_f$ will be taken as a measure of the relative tendency for erodent fragmentation. The smaller D_c/D_f is, the less likely erodent fragmentation relative to target lateral cracking will be. Neglecting E/H, which is approximately a constant for conventional ceramics (≈ 20 to 30), D_c/D_f can be written as

$$\frac{D_c}{D_f} = \text{constant} \left(\frac{\beta_p}{\beta_t}\right)^{-1} \left(\frac{K_p}{K_t}\right)^{-2} \left(\frac{H_p}{H_t}\right)^{2+r} \qquad (8)$$

where $1 \leq 2 + r \leq 5/3$. The hardness ratio H_p/H_t and the fracture toughness ratio K_p/K_t or geometry-flaw ratio β_p/β_t have opposite effects on fragmentation processes. As shown schematically in Fig. 3, an increase in H_p/H_t leads to increased erodent fragmentation while an increase in K_p/K_t or β_p/β_t leads to
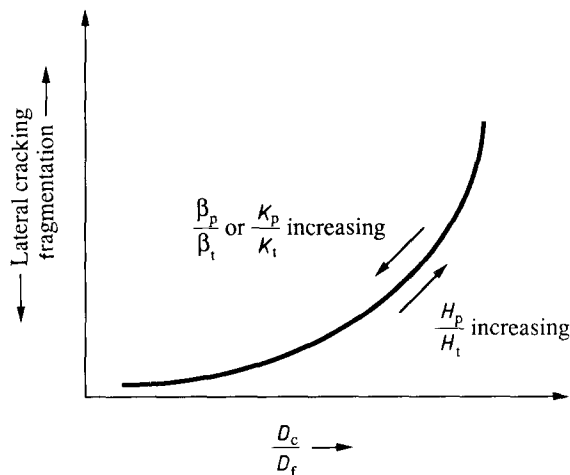

Figure 3 Schematic plot showing the relative trend to erodent fragmentation or target lateral cracking as a function of the D_c/D_f ratio. The effect of the various property ratios in Equation 8 is also indicated.

reduced fragmentation, and enhanced lateral cracking of the target.

The analysis of erosion mechanisms will be based on Equations 5 and 8. The former is a measure of the maximum propagation of lateral cracks via Equation 2 and involves the target material properties, H_t and K_t. The latter is a measure of the relative tendency for erodent fragmentation via fracture initiation and involves a combination of erodent and target property ratios. A direct connection between erodent fragmentation and erosion rate is quite difficult to establish because it depends on the details of the deformation-material removal path (implicitly included in the proportionality constant in Equation 5). It has been suggested that fragmentation will enhance erosion rates through secondary erosion effects [14]. However, fragmentation will also lead to the crushing and blunting of sharp erodent particle tips, diminishing the load transfer characteristics and reducing the efficacy of lateral crack generation. From an energy standpoint, the energy loss in fragmentation must reduce the energy transfer to the target and so reduce erosion rates. Therefore, it appears reasonable to assume that fragmentation can also reduce erosion rates. This is the viewpoint adopted by the current authors.

3. Experimental details
3.1. Material specifications
A series of seven different alumina ceramics with grain size < 10 μm were used. Table I shows the specifications for the different target materials. The fracture toughness values were not measured as part of this investigation but, based on existing data, it can be assumed that these range between about 3.0–3.5 MPa m$^{1/2}$ for the materials used here [15–17]. The toughness of sapphire is about 2.0 MPa m$^{1/2}$. The materials were cut into plate samples measuring 25 mm × 25 mm using a diamond saw. The thickness of the plates varied from 5–8 mm depending on the manufacturer. The erodent particles were alumina (Norton E-17 Alundum) and SiC (Norton 37 Crystolon), hereafter referred to as E17 and SiC, respectively, in 63 and 405 μm sizes. Stereological analysis gave similar size and shape parameters for E17 and SiC [18]. They are both sharp, angular erodent particles with comparable overall topology. Particles of 405 μm SiC and E-17 were cast into metallographic epoxy and polished flat. The hardness was measured using a Micromet hardness tester fitted with a Vickers indentor at a load of 400 g. Similar hardness tests were made on flat, polished plates of the target materials. The hardness of the SiC particles was 25.7 GPa while that of the E17 particles was 16.9 GPa. Table II shows the ratios of the particle-to-target hardness H_p/H_t for both erodents. Toughness data for the erodent particles is not available.

3.2. Experimental procedure
Erosion testing of the samples was conducted using an air-blast type erosion rig [18, 19]. The velocity of the erodent particles in the air stream is controlled by

TABLE I Specifications of alumina target materials

Sample	Supplier	$Al_2O_3^a$ (wt %)	Grain size[b] (μm)	Vickers hardness (GPa-400 g load)
A-459	Kyocera	90	1.51 ± 0.30	8.1
AD-90	Coors	90	2.65 ± 0.43	11.4
AD-995	Coors	95	8.83 ± 1.48	14.6
A-500	Kyocera	98	8.15 ± 2.83	15.4
A-479SS	Kyocera	99.5	7.31 ± 3.88	17.7
A-56	Kyocera	99.7	4.54 ± 1.40	18.2
Sapphire	Saphikon	100	Single crystal	22.2

[a] Manufacturer's specifications.
[b] Samples were polished using Buehler Dialog Method 10.02. The samples A-459, AD-90 and A-500 were chemically etched using 100 % HF. Remaining samples were thermally etched at 1400 °C for 30 min. Grain size was measured by Heyn's intercept method

TABLE II Ratio of particle to target hardness (H_p/H_t)

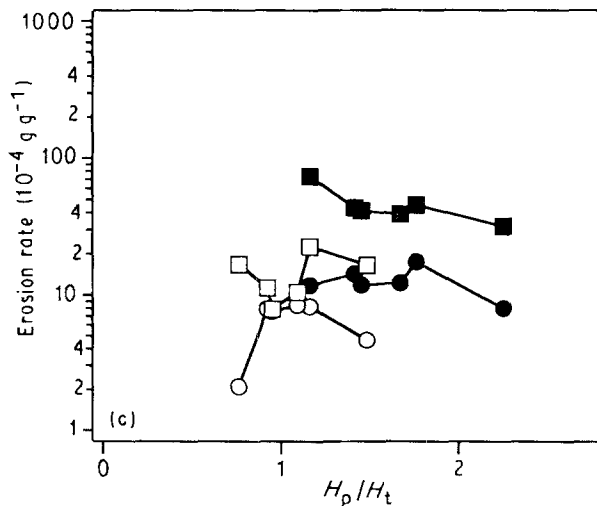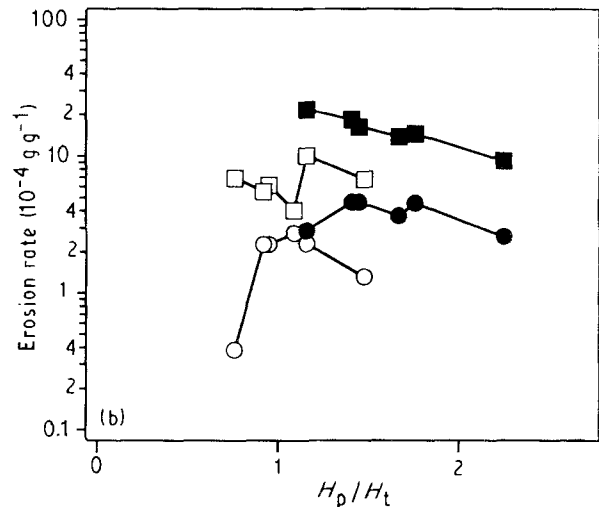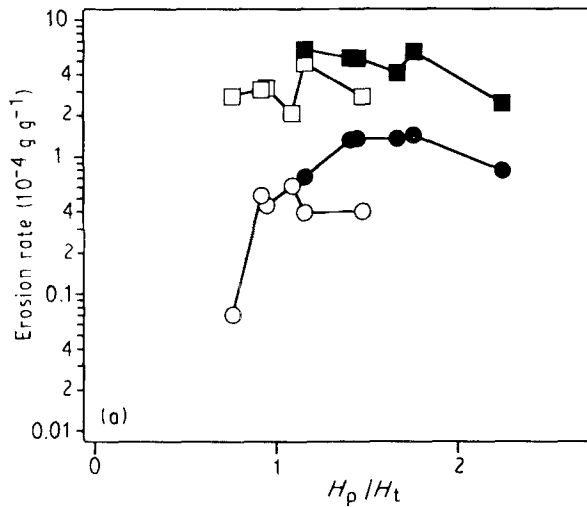| Sample	A-459	AD-90	AD-995	A-500	A-479SS	A-56	Sapphire
E17	2.08	1.48	1.16	1.09	0.95	0.92	0.76
SiC	3.17	2.25	1.76	1.67	1.45	1.41	1.16

Figure 4 Erosion rate plotted against H_p/H_t for the materials listed in Table I. Data for (○, □) E17 and (●, ■) SiC erodents at (○, ●) 63 and (□, ■) 405 μm size are plotted as the four curves indicated in each figure (a–c). Erodent particle velocities, V = (a) 40, (b) 60 and (c) 90 m s^{-1}.

the samples after impact with a preweighed amount of abrasive particles. Testing of the samples was continued until at least three constant weight loss measurements were obtained. A graph of the cumulative weight loss versus dose was plotted and the slope of the graph in the steady state regime gives the steady state erosion rate in gm/gm. Steady state erosion rates for all samples tested are given in Table III. Considerable variability was found in the microstructure for A-459 and erosion-rate measurements did not give consistent results due to sample-to-sample variation. Consequently, data for A-459 is not included in Figs 4–6.

adjusting the pressure of the air. The particle velocity was calibrated using the paddle-wheel method [20]. Velocities of 40, 60, and 90 m s^{-1} were used for testing at normal (90°) impact in all the cases. Erosion of the samples was measured by recording the weight loss of

4. Results and discussion
Fig. 4 shows a plot of the steady state erosion rates versus the hardness ratio, H_p/H_t, for the three test

TABLE III Steady state erosion rates $(10^{-4}\, g\,g^{-1})$

Sample	Erodent	Size (μm)	40 m s^{-1}	60 m s^{-1}	90 m s^{-1}
A-459	SiC	63	1.22	3.70	12.75
	SiC	405	4.38	16.00	49.76
	E17	63	0.68	11.14	24.94
	E17	405	4.68	14.38	31.28
AD-90	SiC	63	0.79	2.58	7.94
	SiC	405	2.45	9.20	31.5
	E17	63	0.40	1.31	4.61
	E17	405	2.73	6.75	16.49
AD-995	SiC	63	1.43	4.55	17.50
	SiC	405	5.85	14.5	45.50
	E17	63	0.39	2.28	8.20
	E17	405	4.83	10.00	22.56
A-500	SiC	63	1.35	3.67	12.25
	SiC	405	4.10	13.83	38.86
	E17	63	0.61	2.73	8.38
	E17	405	2.08	4.03	10.50
A-479SS	SiC	63	1.35	4.60	11.85
	SiC	405	5.20	16.17	41.00
	E17	63	0.44	2.25	7.50
	E17	405	3.18	6.10	7.83
A-56	SiC	63	1.32	4.60	14.22
	SiC	405	5.25	18.25	43.13
	E17	63	0.52	2.25	7.83
	E17	405	3.09	5.50	11.25
Sapphire	SiC	63	0.71	2.85	11.75
	SiC	405	6.08	21.75	73.46
	E17	63	0.07	0.38	2.08
	E17	405	2.75	6.90	16.67

velocities. While some scatter exists, erosion rates generally decrease with increasing H_p/H_t for the aluminas. Sapphire (the smallest H_p/H_t point on each curve) shows an anomalously low erosion rate for 63 μm E17 particles. The erosion rates for SiC are higher than for E17 at a given particle size. Larger size erodents show a larger erosion rate because, even when ΔE is normalized as mass removed/mass impacted, there remains an inherent particle size dependence for ΔE reflected in the size exponent, m. The values of m, based on two particle sizes only, showed some scatter without systematic variation. The measured values were close to the predicted value of $m = 2/3$ (see Appendix) for most cases.

The trend in erosion rates with increasing H_p/H_t can be rationalized in terms of the effect of hardness on lateral crack propagation and erodent fragmentation. For a given erodent, the ratios K_p/K_t and β_p/β_t can be considered constant for the data shown in Fig. 4. The toughness of sapphire is not simply related to that for alumina, as will be noted further later. As seen from Fig. 3, an increase in H_p/H_t leads to increased fragmentation of the impacting erodent particles. This should reduce the effectiveness of lateral crack generation and reduce erosion rates. Decreasing the target hardness, H_t, reduces lateral crack extension, as reflected in Equation 5, reducing erosion rates as H_p/H_t increases (H_t decreases). Both effects lead to decreasing erosion rates with increasing H_p/H_t, which is the general trend observed in Fig. 4. However, some increase in erosion rate could occur because of secondary erosion processes associated with increased frag-

mentation [14] and this would counteract the decreasing trend to some extent. Based on the analysis given here, no sharp transition in erosion rates should occur at $H_p/H_t = 1$, and none is observed in Fig. 4.

While the toughness of erodent particles cannot be measured, based on bulk toughness values, it is reasonable to assume that SiC has a higher toughness than E17. Typical toughness value ranges are 3.0–3.5 MPa m$^{1/2}$ and 3.5–4.5 MPa m$^{1/2}$ for aluminas and SiC, respectively [15–17, 21]. Polycrystalline alumina also shows crack growth resistance behaviour [22], which will reduce the operative toughness for the smaller scale fracture events concomitant with erosion. Given that K_p/K_t is larger for SiC than for E17, Fig. 3 shows that less fragmentation should be expected for the former and the erosion rates should therefore be higher with SiC. The results in Fig. 4 confirm this trend for given erodent particle size and further suggest that fragmentation effects controlled by the K_p/K_t ratio are an important factor in determining erosion rates.

An interesting anomaly arises in Fig. 4 for the 63 μm E17 erodent on sapphire (lowest H_p/H_t value). The erosion rate for 63 μm E17 on sapphire is noticeably low compared to the polycrystalline aluminas. This is not an H_p/H_t transition effect. The low rate can be attributed to crack growth resistance effects (R-curve behaviour). For very small crack-size scales, as pertain to 63 μm erodent impacts, the toughness of sapphire can actually be larger than that of polycrystalline alumina. This results from the fact that, for very short cracks, the toughness in alumina is controlled by

grain boundary fracture toughness. This can be significantly less than that of sapphire (Al_2O_3) single crystal (effective fracture energy for grain-boundary cracks is $\gamma_{eff} = 2\gamma_{surface} - \gamma_{grain\ boundary}$). For longer cracks, the toughness of alumina is controlled by grain-boundary pull-out and grain-bridging processes, leading to a higher fracture toughness than for sapphire single crystal. These crack-size scale effects have been clearly demonstrated in the studies by Cook et al. [22]. The implication for Fig. 4 is that K_t is relatively high and K_p/K_t relatively low for 63 μm E17 impacts on sapphire because of the small crack-size scale (E17 erodent is polycrystalline alumina). In the light of Fig. 3 and Equation 5, this implies increased erodent fragmentation and reduced lateral crack extension. Consequently, the anomalously low erosion rates are observed in Fig. 4 for 63 μm E17 on sapphire. Anomalies in the performance of aluminas due to crack growth resistance behaviour have been reported in the literature in other contexts [23, 24].

An interesting aspect of the erosion behaviour can be analysed without having to predict the absolute value of the erosion rate. This follows by combining the quasi-static analysis for erodent particle contact conditions with the lateral crack controlled erosion model, as outlined earlier. The essential feature of this analysis rests in the assumption that fragmentation effects can be treated as bluntings of sharp erodent particle tips. By considering very sharp (conical) to very blunt (flat-cylinder) shapes, it can be shown that the velocity exponent in Equation 5 decreases with increasing fragmentation (blunting), irrespective of the details of the model assumptions. The results are summarized in the Appendix.

Velocity exponents for the erosion data were obtained by plotting logarithmically the erosion rate against particle velocity (Table III). Very good linear fits were obtained, as is usually the case for ceramics [25] and the exponent, n, in Equation 5 was obtained from such plots. Fig. 5 is a plot of the velocity exponents versus the target hardness, H_t. The results show no systematic correlation with H_p/H_t. However, there is a definite shift in the mean exponent values (horizontal lines) with changes in the erodent particle size. 63 μm particles show higher n values than do 405 μm particles for both SiC and E17. Furthermore, there is a much larger shift in exponents for E17 than for SiC. This inherent "particle-size shift" for velocity exponents can be rationalized on the basis of the geometry-flaw ratio β_p/β_t in Fig. 3. It is reasonable to assume that β_p/β_t decreases for larger erodents because of their higher intrinsic flaw population (size effect for brittle solids). This in turn leads to increased fragmentation and particle-tip blunting for larger erodents, reducing the n values in accord with the quasi-static predictions for particle-tip blunting. That larger size erodents tend to show more fragmentation is in agreement with the studies of Tilly and Sage [14].

The shift in velocity exponents in Fig. 5 is larger for E17 than for SiC. This behaviour is consistent with the expectations in Fig. 3 because K_p/K_t is larger for SiC than for E17. The former has less propensity for fragmentation and particle-tip blunting. It is also possible

that E17 has a larger intrinsic flaw population than SiC and the enhanced fragmentation can result in part from a smaller overall β_p/β_t ratio. Alundum-grade alumina erodents such as E17 are described as being "friable" sharp abrasives by the supplier [26]. The actual magnitude of the velocity exponents in Fig. 5 must be determined by the shape and fragmentation characteristics of the particles. Analysis of E17 and SiC showed that both particles were sharp and angular, with some differences in shape and form factors that may affect the exponent values [18].

The decrease in velocity exponents observed by Sykes et al. [3] is also consistent with a K_p/K_t effect, albeit in a different mode. As the amount of SiC whisker-reinforcement in the alumina matrix composites increased, velocity exponents decreased significantly for an alumina erodent. K_t increases with whisker content in such composites and so K_p/K_t decreases. This enhances fragmentation as whisker content increases (Fig. 3) and reduces the n values. The authors analysed their results in terms of R-curve effects, which can lead to some decrease in the n values [3, 6]. However, it appears that erodent fragmentation is a major factor for the trends observed. Recent results by Routbort [4] indicate that the velocity exponent shift for the composites studied in [3] is smaller for SiC erodents.

Fig. 6 shows a typical plot of the erosion rate versus the inverse grain size for the polycrystalline aluminas. The inverse grain size for sapphire is taken as zero. It can be seen that there is no systematic correlation of the erosion rate with grain size (63 μm E17 on sapphire shows the anomalously low rate discussed earlier). The results do not show the grain size dependence required for Ritter's grain-ejection erosion model [27], thus supporting a lateral crack controlled erosion mechanism.
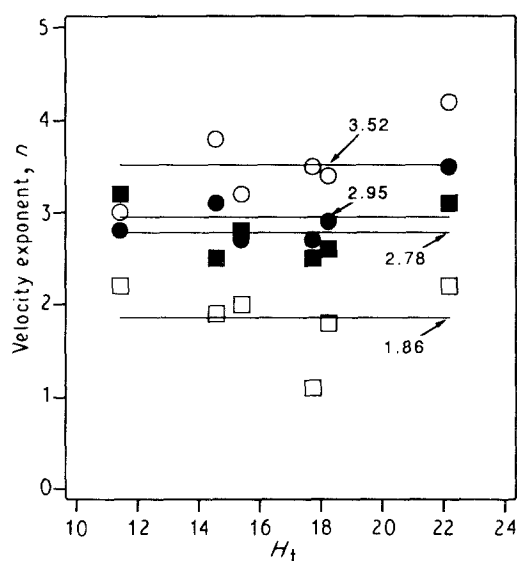

Figure 5 Velocity exponent, n versus target harness (GPa) for the materials listed in Table I. Mean-value horizontal lines are shown with n values indicated. The mean-value velocity exponents are 3.52 and 1.86 for (○) 63 and (□) 405 μm E17, respectively, and 2.95 and 2.78 for (●) 63 and (■) 405 μm SiC, respectively.
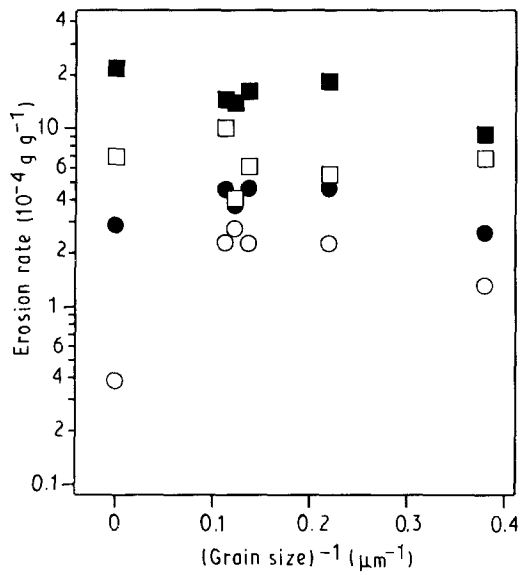
Figure 6 Erosion rate versus inverse mean grain size for the materials listed in Table I. (○) 63 and (□) 405 μm E17; (●) 63 and (■) 405 μm SiC.

Scanning electron microscopy (SEM) observations of single impacts on polished surfaces were made to provide insight into the erosion mechanisms. Typical results for 405 μm E17 and SiC impacts on sapphire are shown in Fig. 7. A plastic-punching type impact with the absence of lateral cracking is seen for E17. SiC impact events under similar conditions showed classic lateral cracking, as can be seen in the figure. Confocal laser microscopy (CLM) was used to measure the width and depth of the plastic-punching zone for the 405 μm E17 impacts as well as the width and depth of the lateral crack zone for SiC impacts. The results shown in Fig. 8 indicate a smaller width and shallower depth for the punching events on sapphire. Similar trends were observed for polycrystalline aluminas impacted with E17 and SiC.

The plastic-punching impacts observed for E17 suggest increased fragmentation due to decreased K_p/K_t for E17 on alumina or sapphire targets. Particle-tip blunting is sufficiently adverse so as to prevent the generation of lateral cracks altogether in this case, leaving only a plastic indentation zone at the impact site. It is clear from this observation that fragmentation should inhibit lateral crack controlled erosion. Direct evidence for particle-tip crushing effects were recently reported by Murugesh and Scattergood [7]. 405 μm erodents were mounted on to microhardness indentor fixtures and used for indentation tests on sapphire plates. Particle-tip crushing and fragmentation was observed using an indentation-replication technique with polished copper as the replicate material. As indentation load increased, fragmentation initiated and became more severe. Although particle-to-particle variation was evident, E17 underwent noticeable fragmentation at lower loads than SiC. It is pertinent to note in this regard that the lower H_p/H_t ratio for E17 on sapphire implies less fragmentation for E17 relative to SiC (Fig. 3), which is contrary to the observation. K_p/K_t thus emerges as a key parameter for fragmentation effects.
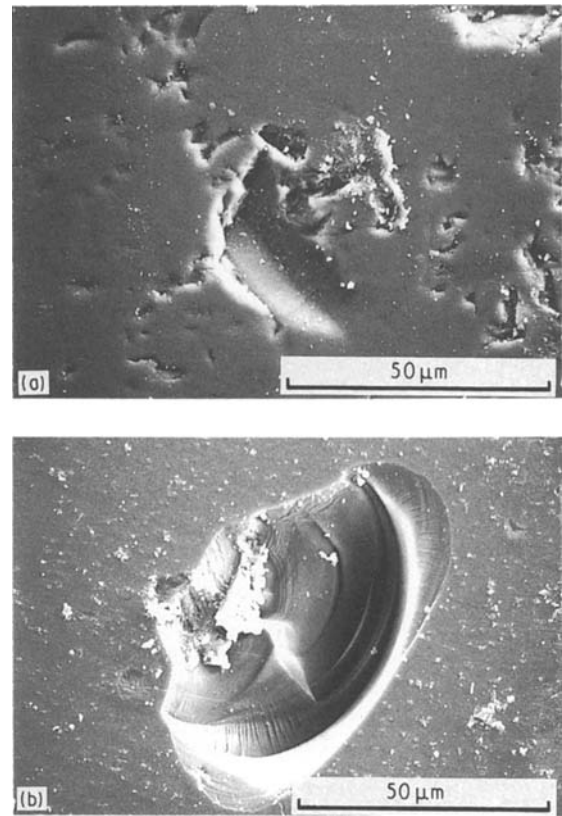

Figure 7 Scanning electron micrographs of single impacts on sapphire at $V = 90$ m s^{-1}. (a) 405 μm E17, and (b) 405 μm SiC.
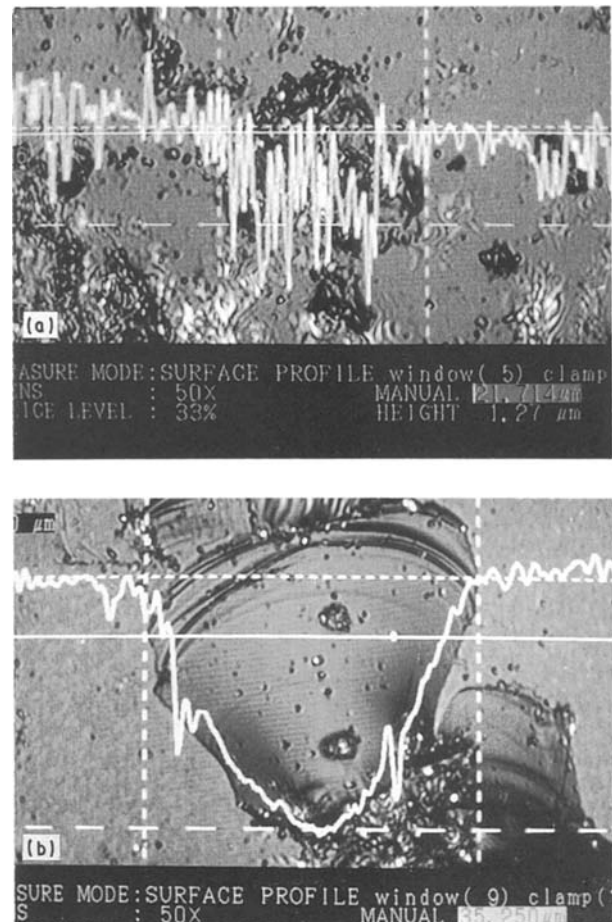

Figure 8 Confocal laser microscope profiles of single impacts on sapphire at $V = 90$ m s^{-1}. (a) 405 μm E17, and (b) 405 μm SiC. The average width, w, and depth, d, of impact events are $w = 57.7$ and 22.1 μm for SiC and E17, respectively, and $d = 5.04$ and 2.95 μm for SiC and E17, respectively.

SEM observations of steady state erosion surfaces offer a quite different picture of erosion mechanisms than do the single impact observations in Figs 7 and 8. In virtually all cases, the steady state surfaces show clear evidence of lateral crack controlled erosion. Furthermore, differences in surface morphologies for E17 versus SiC erodents cannot be detected, in spite of the clear differences noted in Fig. 7. Figs 9 and 10 show typical SEM observations of the steady state surfaces for sapphire and AD995 alumina, eroded under similar conditions with E17 and SiC erodents. The surfaces show the classical features of impact zone debris and lateral crack fracture events. The latter are expected to occur along grain boundaries for the polycrystalline aluminas. In spite of the very similar steady state erosion surface appearance, the differences in erosion rates between E17 and SiC can be large. For example, the 63 μm E17 rate is a factor of 7.5 less than the SiC rate for the surface morphologies shown in Fig. 9.

The similarities in steady state erosion surfaces for E17 and SiC erodents and, in particular, the lateral crack morphology evident in steady state for E17, suggest that the operative erosion mechanism involves a damage accumulation process. Since single impacts of E17 produce plastic-punching, with insufficient plastic zone size (critical penetration depth) to initiate lateral cracks, multiple impacts are needed to build up the requisite zone size for lateral crack generation. Stated otherwise, multiple impacts are needed to drive the plastic zone depth to that corresponding to the critical penetration depth, d_c, for a single impact. Thus, the "average" critical penetration depth event for E17 erodents is actually the accumulation of damage depths from multiple impacts. Nevertheless, the primary material removal mechanism is still the propagation of lateral cracks. The lack of effective lateral crack generation for a single impact event must in turn be related to particle-tip fragmentation and blunting effects. That damage accumulation is necessary is also supported by the fact that, compared to SiC, E17 erodents were observed to display long erosion-rate transients prior to achieving steady state.

Fragmentation and blunting of erodent particle tips also leads to the generation of Hertzian cone (ring) cracks. Hertzian cracks are normally associated only with spherical indentors. The fact that they can be observed for the sharp erodents used here is further evidence of blunting by fragmentation. A Hertzian crack generated by a single impact of a 405 μm E17 particle on sapphire is shown in Fig. 11a. Fig. 11b shows an interesting feature found on steady state erosion surfaces for both sapphire and alumina. The very round "worm-hole" feature observed on sapphire in Fig. 11b cannot be due to microstructural variation such as porosity but instead must be a result of the
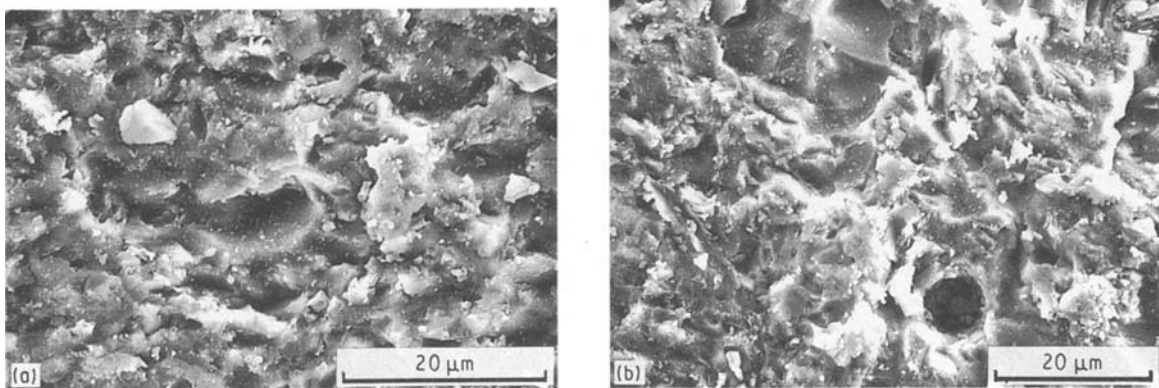

Figure 9 Scanning electron micrographs of steady state erosion surfaces on sapphire at $V = 90 \mathrm{\,m\,s^{-1}}$. (a) 63 μm E17, and (b) 63 μm SiC. Note the round hole appearing in (b) which is discussed in the text.
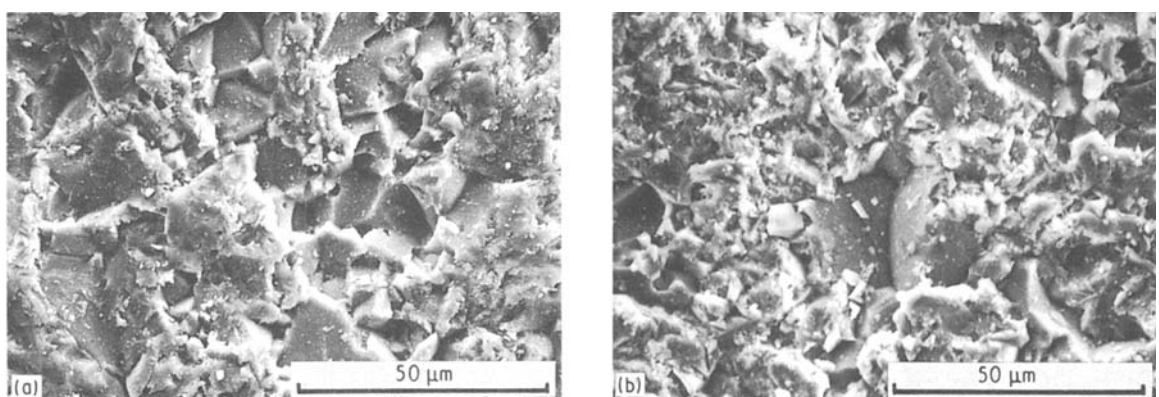

Figure 10 Scanning electron micrographs of steady state erosion surfaces on AD995 alumina at $V = 90 \mathrm{\,m\,s^{-1}}$. (a) 63 μm E17, and (b) 63 μm SiC.
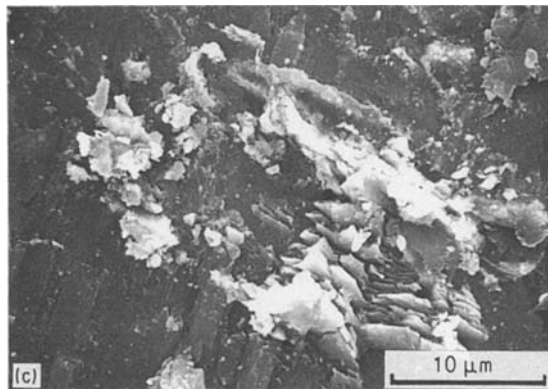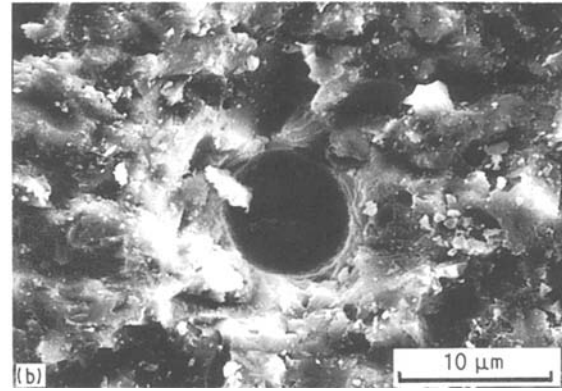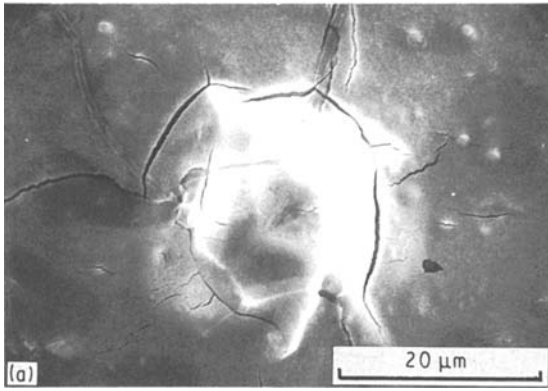
5463

Figure 11 Scanning electron micrographs for 405 μm E17 on sapphire at $V = 90 \, \mathrm{m\,s^{-1}}$. (a) Hertzian type cone cracks about the impact site, (b) "worm-hole" morphology produced by Hertzian and lateral crack interaction as discussed in the text (see also Fig. 9b), and (c) shear bands within the impact site.

interconnection of Hertzian cone cracks with subsurface lateral cracks, removing a circular plug of material (another example can be seen in Fig. 9). Hertzian cone crack effects are consistent with the damage accumulation processes noted earlier because the former are indicative of plastic-punching events occurring simultaneously with lateral crack controlled erosion. Shear band features were occasionally observed on the steady state erosion surfaces in alumina and sapphire. Shear microbands for an impact event on sapphire are shown in Fig. 11c. These are reminiscent of the thermally induced shear-flow instabilities occurring during very high-speed cutting operations [28]. This implies that quite high temperatures can be achieved locally for favourable erosion contact conditions. Furthermore, such shear bands do not require the presence of a glassy second phase in the microstructure.

A comment on the relationship of erodent-to-target properties and the role of H_p/H_t is in order. The interesting results reported by Wada and Watanabe [1] initially suggested that a critical transition point for the erosion behaviour occurred at $H_p/H_t = 1$. Erosion rates increased sharply above this point. No evidence was found in the current investigation to verify this effect, either theoretically or experimentally. In fact, it now appears that the erodent–target toughness properties play a more important role than hardness in dictating phenomena such as reduction in erosion rates due to erodent fragmentation. The previous authors [1] varied H_p/H_t by using a series of different erodents on a given target material. It is likely that the toughness ratio, K_p/K_t, entered into their results and was implicitly included in the H_p/H_t plots. Glass was among the erodents used for the lower H_p/H_t values.

Certainly a lower value of K_p/K_t could suppress erosion rates for glass erodents, and possibly others, through fragmentation effects. For the results obtained here, a fixed erodent and a series of target materials with the same nominal toughness were used to investigate the H_p/H_t effect. K_p/K_t was isolated and the role of H_p/H_t could be more clearly identified.

Finally, while effects related to erodent–particle fragmentation have been used to help rationalize the experimental results, direct measurements of fragmentation during erosion were not made. Such measurements may be possible by careful determination of erodent particle-size distributions taken before and after erosion tests. Because particle-tip crushing can be localized [7], special attention will have to be paid to analysing subtle changes in the fine end of the particle-size distribution curves. Undertaking this kind of study was beyond the scope of the present investigation.

5. Conclusions

The work reported here was aimed at investigating the relationship between erodent and target properties during solid particle erosion for a series of aluminas and sapphire. E17 (alumina) and SiC erodents were used. New models were developed to help elucidate the role of toughness, hardness and erodent fragmentation effects. The results of this investigation support the following conclusions.

1. Using a critical-depth criterion for fracture initiation and recognizing that erodent and target will simultaneously undergo localized plastic deformation at impact, a relative measure of the propensity for erodent fragmentation can be derived. Particle-to-target ratios of hardness, H_p/H_t, toughness, K_p/K_t, and geometry-flaw characteristics, β_p/β_t, play a role in fragmentation phenomena. The amount of fragmentation is predicted to increase as H_p/H_t increases or as K_p/K_t or β_p/β_t decrease.

2. Results obtained for a series of aluminas did not confirm the H_p/H_t effect reported earlier in the literature, where erosion rates increased sharply with increasing H_p/H_t above the transition point $H_p/H_t = 1$. Furthermore, no theoretical basis could be established for such a transition. It appears that the earlier work may implicitly have included K_p/K_t effects that reduced erosion rates by fragmentation, giving the appearance of an H_p/H_t transition point.

3. It is difficult to establish a direct connection between erodent particle fragmentation and steady state erosion rates. The results obtained here are, nevertheless, consistent with a reduction in erosion rate for increased fragmentation. Furthermore, by including particle shape effects in the quasi-static erosion model, it was shown that the blunting of sharp erodents due to fragmentation will reduce velocity exponents. Because of a decrease in β_p/β_t with increasing erodent particle size via flaw population statistics, velocity exponents are expected to decrease as particle size increases. The experimental results confirm this expectation. Because of lower K_p/K_t values, the velocity exponent shift is noticeably greater for E17 erodents than for SiC on aluminas.

4. In certain cases where crack size scales are very small, crack growth resistance effects (R-curve behaviour) can be inferred from the erosion-rate data. In particular, sapphire can have a significantly larger toughness than polycrystalline alumina in the short crack limit, thereby modifying the effective K_t and K_p/K_t, producing anomalously low erosion rates.

5. When conditions are favourable for particle-tip fragmentation, plastic-punching type single impacts are observed on polished surfaces rather than classical lateral cracking. Nevertheless, the steady state erosion surfaces display lateral crack controlled morphology when single impacts under identical conditions produce plastic-punching. Evidently, damage accumulation processes underlie the steady state erosion mechanisms. Multiple plastic-punching impacts build up the requisite critical penetration depth (plastic zone size) needed to generate lateral cracks. The observed erosion rate transients and the existence of Hertzian cone crack damage are consistent with this viewpoint.

Appendix – quasi-static analysis

Erosion models for brittle materials are derived using the centre-loaded penny-crack fracture mechanics analysis for lateral cracks given in Equation 4. This gives the erosion rate ΔE in terms of F_{max} and h. A "contact model" analysis is needed to obtain these quantities in terms of erodent–target properties and kinematic variables such as impact velocity. The quasi-static analysis [9] captures the essential features and is the easiest to develop.

Fig. A1 shows a contact event for a perfectly rigid, sharp, conical-shaped particle. The particle has mean size, R (base radius) and apex angle, 2ψ. For penetration depth, z, the parameters characterizing the contact geometry are

$$V_0 = \text{volume of cone} = \frac{\pi R^3}{3\tan\psi} \qquad \text{(A1a)}$$

$$a = \text{contact radius} = z\tan\psi \qquad \text{(A1b)}$$

$$v = \text{indented volume} = \frac{\pi a^3}{3\tan\psi} \qquad \text{(A1c)}$$

In the quasi-static approximation (no inertial forces), the particle contact force $F(z)$ balances the tractions exerted by the target material and

$$F(z) = \pi a^2 H_t = \pi H_t z^2 \tan^2\psi \qquad \text{(A2)}$$

where H_t is the target hardness (in principle, strain-rate effects should be included in H_t and K_t). The analysis is carried out here for normal impact, because this is the case used for the experiments. Further assumptions are needed to deal with oblique impact, for example, only the normal component of the contact force contributes to erosion. It is then assumed that the plastic work done is a fixed fraction of the particle kinetic energy so that

$$W_{plastic} = \int_0^{z_{max}} F(z)\,\mathrm{d}z = \gamma KE$$

$$= \gamma\frac{1}{2}\rho_p V_0 V^2 \qquad \text{(A3)}$$

where ρ_p is the particle density and γ is a transfer coefficient equal to the fraction of kinetic energy used in plastic deformation work. Substituting and evaluating the integral, while for simplicity combining all unnecessary geometric factors into the proportionality constants, one obtains

$$z_{max} = \text{constant } \rho_p^{1/3} H_t^{-1/3} R V^{2/3} \qquad \text{(A4a)}$$

$$v_{max}^{1/3} = \text{constant } \rho_p^{1/3} H_t^{-1/3} R V^{2/3} \qquad \text{(A4b)}$$

$$F_{max} = \text{constant } \rho_p^{2/3} H_t^{1/3} R^2 V^{4/3} \qquad \text{(A4c)}$$

where V is the erodent velocity, R is the size, ρ_p is particle density and H_t is target harness. $v_{max}^{1/3}$ represents the mean size of the maximum indented volume. For other than the conical shape, z_{max} and $v_{max}^{1/3}$ will not involve the same combination of exponents as in Equation A4. For development of the erosion model in Equation 5, scaling-law assumptions are made such that the residual tensile force, P, is proportional to F_{max} and the depth, h, is proportional to either z_{max} or $v_{max}^{1/3}$ as indicated in Equation 3. Residual tensile force results because of the plastic constraint existing after elastic unloading, as has been documented by indentation studies [10, 11]. It is the residual tensile force that
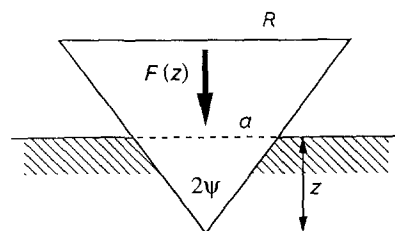

Figure A1 Schematic diagram of the impact of a conical-shape erodent particle.

TABLE AI Parameters and relations from quasi-static analysis. Proportionality constants are omitted for z_{max}, etc. The exponents s, q, m and n pertain to Equation 5. The right-hand side of Equation 5 is divided by $R^3 \rho_p$ to obtain the values of s, q, m and p shown for ΔE in mass/mass

Shape	z_{max}	$v_{max}^{1/3}$	F_{max}	$\Delta E_1 (h = z_{max})$				$\Delta E_2 (h = v_{max}^{1/3})$			
				s	q	m	n	s	q	m	n
Cone	$\rho_p^{1/3} H_t^{-1/3} R V^{2/3}$	$\rho_p^{1/3} H_t^{-1/3} R V^{2/3}$	$\rho_p^{2/3} H_t^{1/3} R^2 V^{4/3}$	2/9	1/9	2/3	22/9	2/9	1/9	2/3	22/9
Sphere	$\rho_p^{1/2} H_t^{-1/2} R V$	$\rho_p^{1/3} H_t^{-1/3} R V^{2/3}$	$\rho_p^{1/2} H_t^{1/2} R^2 V$	1/6	2/3	2/3	7/3	0	1/3	2/3	2
Cylinder	$\rho_p H_t^{-1} R V^2$	$\rho_p^{1/3} H_t^{-1/3} R V^{2/3}$	$H_t R^2$	0	1/3	2/3	2	$-2/3$	1	2/3	2/3

drives the lateral cracks which cause erosive material loss. Substituting Equation A4 into Equation 5 results in the final phenomenological form for the erosion rate given in Equation 5. The right-hand side of Equation 5 should be divided by $\rho_p R^3$ to obtain ΔE as mass target eroded/mass erodent impacted. Target density is essentially constant for the aluminas used here and is omitted.

An interesting trend can be obtained from the quasi-static analysis by varying the particle shape from conical (very sharp) to spherical to flat-cylindrical (very blunt). The analysis is carried out just as indicated above but with appropriate changes in the geometry relations. Full details have been given elsewhere [18]. The results are summarized in Table AI. The particle shape trends in ΔE are independent of model assumptions ($h = z_{max}$ or $v_{max}^{1/3}$) but the actual numerical values for the power-law exponents will vary. In particular, notice that the particle size exponent is fixed at $m = 2/3$ while the velocity exponent, n, decreases as particle shape changes from sharp to blunt. Using $h = v_{max}^{1/3}$, n decreases from 22/9 to 2/3. Velocity exponent trends from the model analysis can be used to rationalize the fragmentation effects, as discussed in the text. Fracture toughness enters as $K_t^{-4/3}$ in all cases while target hardness, H_t, varies as shown in Table AI. A weak dependence on erodent particle density, ρ_p, is also shown. Density corrections to the experimental data were not made here, and the values reported in Table III are mass/mass, as is measured directly in the testing procedure.

References

1. S. WADA and N. WATANABE, Yogyo-Kyokai-Shi 95(6) (1987) 573.
2. S. WADA, N. WATANABE and T. TANI, J. Ceram. Soc. Jpn Inter. Edn. 96 (1988) 737.
3. M. T. SYKES, R. O. SCATTERGOOD and J. L. ROUTBORT, Composites 18(2) (1987) 153.
4. J. L. ROUTBORT, private communication (1989).
5. C. T. MORRISON, J. L. ROUTBORT and R. O. SCATTERGOOD, in Materials Research Society Symposia Proceedings, Boston, December 1986, edited by P. F. Becher, M. V. Swain and S. Somiya, 78 (1987) p. 153.
6. S. SRINIVASAN and R. O. SCATTERGOOD, Wear 128 (1988) 139.
7. L. MURUGESH and R. O. SCATTERGOOD, ibid. 141 (1990) 115
8. A. G. EVANS, M. E. GULDEN and M. E. ROSENBLATT, Proc. Roy. Soc. A361 (1978) 343.
9. S. M. WIEDERHORN and B. R. LAWN, J. Amer. Ceram. Soc. 62 (1979) 66.
10. B. R. LAWN and R. WILSHAW, J. Mater. Sci. 10 (1975) 1049.
11. Idem. "Fracture of Brittle Solids", Cambridge Press (1975).
12. K. KENDALL, Proc. Roy. Soc. 361A (1978) 245.
13. B. R. LAWN and A. G. EVANS, J. Mater. Sci. 12 (1977) 2195.
14. G. P. TILLY and W. SAGE, Wear 16 (1970) 447.
15. P. C. SMITH, Mech. Engng January (1987) 25.
16. W. R. EAST, ibid. August (1987) 45.
17. S. WADA and N. WATANABE, Yogyo-Kyokai-Shi 95(9) (1987) 5.
18. L. MURUGESH, MS thesis, North Carolina State University (1989).
19. K. ANAND, S. K. HOVIS, H. CONRAD and R. O. SCATTERGOOD, Wear 118 (1987) 243.
20. S. K. HOVIS, K. ANAND, H. CONRAD and R. O. SCATTERGOOD, ibid. 101 (1985) 69.
21. Z. LI, A. GHOSH, A. S. KOBAYASHI and R. C. BRADT, J. Amer. Ceram. Soc. 72(6) (1989) 904.
22. R. F. COOK, C. J. FAIRBANKS, B. R. LAWN and Y. W. MAI, J. Mater. Res. 2 (1987) 345.
23. S. J. CHO, B. J. HOCKEY, B. R. LAWN and S. J. BENNISON, J. Amer. Ceram. Soc. 72 (1989) 1249.
24. D. B. MARSHALL, B. R. LAWN and R. F. COOK, ibid. 70 (1987) C-139.
25. A. W. RUFF and S. M. WEIDERHORN, Treatise Mater. Sci. Tech. 16 (1979) 69.
26. Norton Alundum Abrasives, Norton Co., Materials Division, Worcester, MA.
27. J. E. RITTER, Mater. Sci. Engng 71 (1985) 195.
28. M. G. SCHINKER and W. DOLL, SPIE Proc. 381 (1983) 32.